

Adjoint-based airfoil optimization with discretization error control

D. Li and R. Hartmann^{*,†}

*Institute of Aerodynamics and Flow Technology, DLR (German Aerospace Center), Lilienthalplatz 7,
38108 Braunschweig, Germany*

SUMMARY

In this article, we develop a new airfoil shape optimization algorithm based on higher-order adaptive DG methods with control of the discretization error. Each flow solution in the optimization loop is computed on a sequence of goal-oriented h -refined or hp -refined meshes until the error estimation of the discretization error in a flow-related target quantity (including the drag and lift coefficients) is below a prescribed tolerance. Discrete adjoint solutions are computed and employed for the multi-target error estimation and adaptive mesh refinement. Furthermore, discrete adjoint solutions are employed for evaluating the gradients of the objective function used in the CGs optimization algorithm. Furthermore, an extension of the adjoint-based gradient evaluation to the case of target lift flow computations is employed. The proposed algorithm is demonstrated on an inviscid transonic flow around the RAE2822, where the shape is optimized to minimize the drag at a given constant lift and airfoil thickness. The effect of the accuracy of the underlying flow solutions on the quality of the optimized airfoil shapes is investigated. Copyright © 2014 John Wiley & Sons, Ltd.

Received 20 May 2014; Revised 8 October 2014; Accepted 11 October 2014

KEY WORDS: discontinuous Galerkin methods; optimization; error estimation; adaptive mesh refinement; hp -refinement; adjoint approach

1. INTRODUCTION

With the fast development of computer technology and numerical methods, the shape optimization based on CFD is playing an increasingly important role in aerodynamic design [1–10]. Given that many flow computations are required within an optimization process, it is important that efficient but still accurate numerical methods are used. Although it is now widely accepted that adaptive mesh refinement is required for an accurate and efficient flow simulation, most aerodynamic shape optimization chains are still based on a fixed computational mesh. There are several reasons for this.

The first reason is related to grid generation. Already for a single airfoil shape and fixed flow conditions, it is difficult to generate *a priori*, that is, before knowing the flow solution, an efficient (and thus necessarily solution adapted) mesh. The situation is significantly more difficult when airfoil shapes and/or flow conditions change during an optimization process. Given that important flow features such as shock strength, shock position, and position of stagnation points change under changing airfoil shapes or flow conditions, the task of generating a mesh *a priori* which is appropriate for a range of airfoil shapes and flow conditions *without* spending too many mesh points in unimportant regions is virtually impossible. Therefore, in practice, typically fixed computational meshes are chosen which are fine enough to (hopefully) capture the most important flow features but are also coarse enough to still be feasible in terms of computational cost within the

^{*}Correspondence to: R. Hartmann, Institute of Aerodynamics and Flow Technology, DLR (German Aerospace Center), Lilienthalplatz 7, 38108 Braunschweig, Germany.

[†]E-mail: ralf.hartmann@dlr.de

optimization process. With this, however, the computational grid remains a compromise between accuracy and efficiency.

A solution to this problem could be the use of adaptive mesh refinement, in particular, the use of adaptive mesh refinement which is tailored to the accurate and efficient computation of the aerodynamic forces for the flow problem at hand. For the different flow solutions (different shock positions, etc) obtained for different airfoil shapes and flow conditions, this, however, leads to different solution adapted meshes. Thereby, each functional evaluation in the optimization process will be based on a different computational mesh.

This gives rise to the second problem, namely, the problem as how to distinguish between the differences obtained in the optimization process due to changes in the airfoil shape from the differences obtained through the change of the locally refined computational mesh. Again, in practice, this problem is (supposedly) avoided by simply using a fixed computational mesh and thus removing mesh dependency. This approach stands and falls with the assumption that the discretization error would behave ‘similarly’ on the same mesh for the range of airfoil shapes and flow conditions under consideration. In fact, however, the discretization error depends on the mesh as well as on the flow solution. Thus, even with a fixed computational mesh, the functional evaluations in an optimization process are subject to discretization errors of different error levels.

In this work, we propose a new approach of aerodynamic shape optimization addressing both problems outlined earlier. In particular, we employ adaptive higher-order DG methods [11–13], which come along with a strong mathematical and practical background in error estimation and adaptive mesh refinement. Given a target quantity such as an aerodynamic force (e.g., drag, lift or moment) coefficient, an associated discrete adjoint solution can be computed and used to evaluate so-called adjoint-based indicators. Used in an adaptive mesh refinement algorithm, these indicators are tailored to the accurate and efficient approximation of the target quantity (cf. [14, 15] and the references cited therein). Furthermore, they sum up to an *a posteriori* error estimate which provides an approximation of the discretization error in the computed force coefficient on the current adapted mesh and flow solution. If each flow solution in the optimization process is adapted and computed until a specific tolerance in the discretization error is reached, then the discretization error is ‘under control’. Then the flow solution and derived quantities are comparable, and larger differences in computed quantities for different airfoil shapes are significant in the sense that they can, in fact, be attributed to the change in the airfoil shape.

Although the incorporation of adjoint-based error estimation and goal-oriented mesh refinement in optimization problems is well-established techniques for finite element discretizations of incompressible flow control problems [16, 17], up to now, only few authors incorporated adaptive mesh refinement and error control in aerodynamic shape optimization processes. Lu [18, 19] considered a volume and lift-constrained airfoil drag minimization problem where he added the constraints as penalties to the objective function. He employed a DG flow solver within the gradient-based Broyden-Fletcher-Goldfarb-Shanno (BFGS) quasi-Newton optimization method where he incorporated error estimation based on concurrent flow and adjoint solutions in combination with adjoint-based local p -refinement for the drag coefficient. Later, Nemec and Aftosmis [20] built on Lu’s ideas and considered a lift-constrained inverse design problem in the area of sonic-boom control. For this, they employed a second-order finite volume solver, realized the lift constraint also as penalty function, and employed adjoint-based mesh refinement for the lift coefficient. However, Nemec and Aftosmis [20] did not control the numerical error but used a fixed number of refinement steps. Furthermore, authors in [18–20] did not investigate the effect of the accuracy of the underlying flow solutions on the quality of the optimized airfoil shapes.

A few other authors also combined mesh adaptation with optimization. Mohammadi and Hecht [21] used an unstructured CAD-free shape optimization framework and automatic differentiation in reverse mode and combined it with adaptive remeshing based on the Hessian metric. More recently, Kouhi *et al.* [22] introduced an adaptive remeshing algorithm using the first and second derivative-based error indicators into a genetic algorithm optimization loop and demonstrated that a better final airfoil shape is obtained on adapted meshes than on uniform fixed fine meshes. Both, [21, 22], considered a lift and volume-constrained airfoil drag minimization problem with constraints treated as penalty and demonstrated a reduction in the shock strength of the transonic flow and in the drag.

However, both works neither employed goal-oriented mesh refinement but feature-based refinement nor did they consider error control.

The current work is based on the DLR flow solver PADGE [23], which implements higher order and adaptive DG methods for aerodynamic flows. This includes the solution of the flow problems and of associated adjoint problems for the evaluation of the adjoint-based *a posteriori* error estimation and indicators for goal-oriented mesh refinement. These indicators can be used for pure mesh refinement (*h*-refinement) as well as for mesh refinement combined with a local variation of the polynomial degree *p* resulting in so-called (*hp*-refinement) For smooth flow solutions, high-order discretization methods have the advantage of providing the same accuracy for a much lower number of DOF and possibly lower computational cost than the second-order discretization methods [24–26]. On top of that, using *hp*-refinement allows to gain from higher polynomial degrees and thus higher discretization orders in smooth parts of the solution while using low polynomial degrees combined with local mesh refinement (*h*-refinement) in non-smooth parts of the solution such as near shocks [27, 28]. We note that in a series of publications over the last decade (cf. [15, 29–31] among others), it has been demonstrated that the implemented adaptation algorithms in the PADGE code are reliable and efficient.

In this work, we now consider an aerodynamic shape optimization where the drag of an airfoil is minimized at a prescribed constant target lift. In this lift-constrained drag minimization problem, the lift constraint is realized by an automatic adjustment of the angle of attack during the flow solution process. Each flow computation in the optimization loop is computed on a sequence of goal-oriented *h*-refined or *hp*-refined meshes until the error estimation of the discretization error in a flow-related target quantity (including the drag and lift coefficients) is below a prescribed tolerance. As both, the drag and lift coefficient, need to be computed accurately in the target lift computations, a multi-target error estimation and adaptation algorithm [30] is used. The CG optimization algorithm [32] is employed where the gradients are evaluated via the adjoint approach [1, 33], which is very efficient in high-dimensional design spaces. Furthermore, an extension of the adjoint-based gradient evaluation to the case of target lift flow computations is employed [2]. The proposed algorithm is demonstrated for an inviscid transonic flow around the RAE2822 airfoil where the airfoil shape is optimized to minimize the drag at a prescribed constant target lift. We will compare the efficiency and accuracy of *hp*-refinement against *h*-refinement within the optimization process. Furthermore, we will investigate the effect of the accuracy of the underlying flow solutions (controlled through the prescribed error tolerance) on the quality of the optimized airfoil shapes.

This paper is structured as follows. After introducing the discretization of the flow and adjoint equations in Section 2, we shortly recall the approach of single-target and multi-target error estimation and adjoint-based mesh refinement in Section 3. In Section 4, we give details on the evaluation of gradients using the adjoint approach including the extension to the treatment of lift constraints and validate the gradients obtained against finite differences on an *h*-refined and an *hp*-refined mesh. Finally, in Section 5, we apply the proposed shape optimization algorithm including error control and mesh refinement on the lift-constrained drag minimization of a transonic inviscid flow around the RAE2822 airfoil and compare the quality of the airfoil shapes optimized on *h*-refined and *hp*-refined meshes for different error tolerances with that on a fixed fine mesh.

2. THE DISCRETE FLOW AND ADJOINT EQUATIONS

We consider the steady-state compressible Euler equations

$$\nabla \cdot \mathcal{F}^c(\mathbf{u}) = 0 \text{ in } \Omega \subset \mathbb{R}^2, \quad \mathbf{v} \cdot \mathbf{n} = v_1 n_1 + v_2 n_2 = 0 \text{ on } \Gamma_W, \quad (1)$$

subject to vanishing normal velocity (slip-wall) boundary conditions on the wall boundary Γ_W with outward unit normal vector \mathbf{n} , where $\mathbf{v} = (v_1, v_2)^\top$ is the velocity vector and \mathbf{u} is the vector of conservative variables $\mathbf{u} = (\rho, \rho v_1, \rho v_2, \rho E)^\top$. Furthermore, we consider the following target quantity

$$J(\mathbf{u}) = \int_{\Gamma_W} p(\mathbf{u}) \mathbf{n} \cdot \boldsymbol{\psi} \, ds, \quad (2)$$

which represents the drag or lift coefficient, depending on the direction $\boldsymbol{\psi}$ given by $\boldsymbol{\psi}_d = \frac{1}{C_\infty} (\cos(\alpha), \sin(\alpha))^\top$ or $\boldsymbol{\psi}_l = \frac{1}{C_\infty} (-\sin(\alpha), \cos(\alpha))^\top$, respectively, where α is the angle of attack, $C_\infty = q_\infty \bar{l}$, where \bar{l} denotes a reference length, $q = \frac{1}{2} \rho |\mathbf{v}|^2$ denotes the dynamic pressure, and subscripts ∞ indicate the freestream quantities. Furthermore, $p(\mathbf{u})$ is the pressure determined by the equation of state of an ideal gas, $p(\mathbf{u}) = (\gamma - 1) (\rho E - \frac{1}{2} \rho \mathbf{v}^2)$. Then the associated continuous adjoint equations are given by

$$-(\mathcal{F}_u^c[\mathbf{u}])^\top \nabla \mathbf{z} = 0 \quad \text{in } \Omega, \quad n_1 z_2 + n_2 z_3 = \mathbf{n} \cdot \boldsymbol{\psi} \quad \text{on } \Gamma_W, \quad (3)$$

(cf. [33, 34]), where \mathcal{F}_u^c denotes the derivative of the convective flux $\mathcal{F}^c(\mathbf{u})$ with respect to \mathbf{u} .

Let the domain Ω be subdivided into shape-regular meshes $\mathcal{T}_h = \{\kappa\}$ consisting of (possibly curved) quadrilateral elements κ . Let us assume that each $\kappa \in \mathcal{T}_h$ is a smooth bijective image of the unit reference square $\hat{\kappa}$, that is, $\kappa = \sigma_\kappa(\hat{\kappa})$ for each $\kappa \in \mathcal{T}_h$. On the reference element $\hat{\kappa}$, we define the space of complete polynomials P_p of degree $p \geq 0$ by $P_p = \text{span}\{\hat{\mathbf{x}}^\alpha : 0 \leq |\alpha| \leq p\}$. We now introduce the finite element space \mathbf{V}_h^p consisting of discontinuous piecewise polynomial functions

$$\mathbf{V}_h^p = \{\mathbf{v}_h \in [L^2(\Omega)]^4 : \mathbf{v}_h|_\kappa \circ \sigma_\kappa \in [P_p(\hat{\kappa})]^4, \kappa \in \mathcal{T}_h\},$$

where h and p indicate the local elemental mesh spacing and polynomial degree, respectively, and are not necessarily uniform throughout the mesh. Then the discretization of (1) is given by the following: find $\mathbf{u}_h \in \mathbf{V}_h^p$ such that

$$N_h(\mathbf{u}_h, \mathbf{v}_h) = 0 \quad \forall \mathbf{v}_h \in \mathbf{V}_h^p. \quad (4)$$

A detailed description of the semilinear form $N_h(\cdot, \cdot)$ can be found in, for example, [34]. Given a target quantity $J(\cdot)$ such as the drag or lift coefficient (2) and a consistent discretization $J_h(\cdot)$ of $J(\cdot)$ (cf. [34]), then the associated discrete adjoint problem is given as follows: find $\bar{\mathbf{z}}_h \in \bar{\mathbf{V}}_h^p$ such that

$$N'_h[\mathbf{u}_h](\mathbf{w}_h, \bar{\mathbf{z}}_h) = J'_h[\mathbf{u}_h](\mathbf{w}_h) \quad \forall \mathbf{w}_h \in \bar{\mathbf{V}}_h^p, \quad (5)$$

where $N'_h[\mathbf{u}_h](\mathbf{w}_h, \bar{\mathbf{z}}_h)$ and $J'_h[\mathbf{u}_h](\mathbf{w}_h)$ are the Fréchet derivatives of $N_h(\mathbf{u}_h, \mathbf{v}_h)$ and $J_h(\mathbf{u}_h)$, respectively, at \mathbf{u}_h in the direction of \mathbf{w}_h . We note that solutions to discrete adjoint problems of the form (5) will be required for three purposes: for adjoint-based error estimation (cf. Section 3), for adjoint-based adaptation (cf. Section 3), and for the evaluation of gradients of the objective function (cf. Section 4) required in a gradient-based optimization algorithm. Depending on the purpose of the adjoint solution, the adjoint discrete function space $\bar{\mathbf{V}}_h^p$ in (5) is given by $\bar{\mathbf{V}}_h^p = \mathbf{V}_h^p$ or $\bar{\mathbf{V}}_h^p = \mathbf{V}_h^{p+1}$. We note that the chosen discretizations $N_h(\cdot, \cdot)$ and $J_h(\cdot)$ of (1) and $J(\cdot)$ are adjoint consistent (cf. [18, 34]), that is, the discrete adjoint problem (5) is a consistent discretization of the continuous adjoint equations (3).

In order to simplify notation in Section 4, we transfer the discrete problems (4) and (5) into vector notation. Rewriting the discrete flow and adjoint solutions $\mathbf{u}_h, \mathbf{z}_h \in \mathbf{V}_h^p$ as linear combinations of the basis functions spanning the discrete function space, that is, $\mathbf{V}_h^p = \text{span}\{\boldsymbol{\phi}_i, i = 1, \dots, N\}$ where N denotes the dimension of \mathbf{V}_h^p , we obtain $\mathbf{u}_h = \sum_{i=1}^N u_i \boldsymbol{\phi}_i$ and $\mathbf{z}_h = \sum_{i=1}^N \lambda_i \boldsymbol{\phi}_i$ and can represent \mathbf{u}_h and \mathbf{z}_h by their associated coefficient vectors $\mathbf{U} = (u_i)_{i=1}^N$ and $\boldsymbol{\lambda} = (\lambda_i)_{i=1}^N$, respectively. Furthermore, defining the residual vector $\mathbf{R}(\mathbf{U}) = (R_i)_{i=1}^N$ with $R_i = -N_h(\mathbf{u}_h, \boldsymbol{\phi}_i)$ and rewriting $\left(\frac{\partial J}{\partial \mathbf{U}}\right)_i = J'_h[\mathbf{u}_h](\boldsymbol{\phi}_i)$, the discrete flow and adjoint equations, (4) and (5), can shortly be written as follows:

$$\mathbf{R}(\mathbf{U}) = 0, \quad -\left(\frac{\partial \mathbf{R}}{\partial \mathbf{U}}\right)^\top \boldsymbol{\lambda} = \left(\frac{\partial J}{\partial \mathbf{U}}\right)^\top. \quad (6)$$

3. ADJOINT-BASED ERROR ESTIMATION AND ADAPTIVE MESH REFINEMENT

The proceeding *a posteriori* estimation of the discretization error based on a duality argument follows the general approach developed by Johnson *et al.* [35], Rannacher *et al.* [36, 37], and Giles *et al.* [38, 39]. The particular form of the adjoint-based refinement indicators is according to [29, 30].

Given the discretization (4) of the flow, Equation 1, and a consistent discretization $J_h(\cdot)$ of the target quantity $J(\cdot)$ in (2), then the discretization error measured in terms of the target quantity, that is, the difference between the exact (but unknown) target quantity value, $J(\mathbf{u})$, and the computed one, $J_h(\mathbf{u}_h)$, is given by the following *error representation*

$$J(\mathbf{u}) - J_h(\mathbf{u}_h) = R_h(\mathbf{u}_h, \mathbf{z}), \quad (7)$$

where $R_h(\mathbf{u}_h, \mathbf{z}) := -N_h(\mathbf{u}_h, \mathbf{z})$ includes the primal residuals multiplied by the exact (but again unknown) solution \mathbf{z} to the (continuous) adjoint problem (3). Replacing the exact adjoint solution \mathbf{z} in (7) by an approximation, namely, the solution $\bar{\mathbf{z}}_h \in \bar{\mathbf{V}}_h^p$ to the discrete adjoint problem (5), we obtain the following approximate error representation, or *a posteriori* error estimate,

$$J(\mathbf{u}) - J_h(\mathbf{u}_h) \approx R_h(\mathbf{u}_h, \bar{\mathbf{z}}_h). \quad (8)$$

Note that due to (4), we have $R_h(\mathbf{u}_h, \mathbf{v}_h) = -N_h(\mathbf{u}_h, \mathbf{v}_h) = 0$ for all $\mathbf{v}_h \in \mathbf{V}_h^p$; in particular, we have $R_h(\mathbf{u}_h, \mathbf{z}_h) = 0$ for any $\mathbf{z}_h \in \mathbf{V}_h^p$. Thus, using an equal-order discrete adjoint solution, that is, $\bar{\mathbf{z}}_h \in \bar{\mathbf{V}}_h^p$ being chosen in the same discrete function space $\bar{\mathbf{V}}_h^p = \mathbf{V}_h^p$ as the flow solution $\mathbf{u}_h \in \mathbf{V}_h^p$, would result in a vanishing (and thus useless) error estimate (7). Instead, if the discrete adjoint space is chosen $\bar{\mathbf{V}}_h^p \not\subset \mathbf{V}_h^p$ then we have $R_h(\mathbf{u}_h, \bar{\mathbf{z}}_h) \neq 0$. Furthermore, if $\bar{\mathbf{V}}_h^p$ is chosen sufficiently large, such as with a higher polynomial degree, $\bar{\mathbf{V}}_h^p = \mathbf{V}_h^{p+1}$, then (8) is an accordingly good approximation to the exact discretization error (7). In a series of publications (e.g., [29, 31] and the references cited in the review [15]), it has been demonstrated that (8) for $\bar{\mathbf{z}}_h \in \bar{\mathbf{V}}_h^p = \mathbf{V}_h^{p+1}$ gives accurate and reliable estimates of the discretization error (7) measured in aerodynamic force coefficients. Furthermore, we note that the error estimate (8) can be localized

$$J(\mathbf{u}) - J_h(\mathbf{u}_h) \approx R_h(\mathbf{u}_h, \bar{\mathbf{z}}_h) \equiv \sum_{\kappa \in \mathcal{T}_h} \bar{\eta}_\kappa, \quad (9)$$

where $|\bar{\eta}_\kappa|$ are the local error indicators including the primal local residuals weighted with the discrete adjoint solution, denoted as *adjoint-based indicators* [31] or as *dual-weighted-residual indicators* [37]. These indicators can be used to drive an adaptive mesh refinement (and coarsening) algorithm specifically tailored to the accurate and efficient approximation of the target quantity $J(\mathbf{u})$. The resulting adaptive mesh refinement is significantly more efficient than global mesh refinement. It has been demonstrated by many authors (cf. [14, 15] and the references cited therein) that using the adjoint-based indicators for mesh refinement is more efficient in accurately approximating $J(\mathbf{u})$ than using indicators which include the primal residuals only or when using even simpler *ad-hoc* indicators.

Given that in the current work, we are concerned with a lift-constrained airfoil drag minimization problem, there is not a single target quantity but (at least) two quantities, namely, the drag and lift coefficients, which need to be approximated accurately and efficiently. Therefore, we employ the approach of multi-target error estimation and adaptivity as described in [30]. In particular, given N target quantities $J_i(\mathbf{u})$, we define a combined target quantity $J_c(\mathbf{u})$ as a linear combination of the original target quantities, $J_c(\mathbf{u}) = \sum_i \omega_i J_i(\mathbf{u})$, with weighting factors $\omega_i = \alpha_i s_i$, $\alpha_i > 0$ (cf. [30] for more details), such that

$$J_c(\mathbf{u}) - J_{c,h}(\mathbf{u}_h) = \sum_i \alpha_i |J_i(\mathbf{u}) - J_{i,h}(\mathbf{u}_h)| \quad (10)$$

and define the following discrete adjoint problem associated to the combined target quantity $J_c(\cdot)$: find $\bar{\mathbf{z}}_{c,h} \in \bar{\mathbf{V}}_h^p$ such that

$$N'_h[\mathbf{u}_h](\mathbf{w}_h, \bar{\mathbf{z}}_{c,h}) = J'_{c,h}[\mathbf{u}_h](\mathbf{w}_h) \quad \forall \mathbf{w}_h \in \bar{\mathbf{V}}_h^p, \quad (11)$$

with $\bar{\mathbf{V}}_h^p = \mathbf{V}_h^{p+1}$ like before. Then the resulting estimate of the discretization error measured in terms of the combined target quantity is given by

$$J_c(\mathbf{u}) - J_{c,h}(\mathbf{u}_h) \approx R_h(\mathbf{u}_h, \bar{\mathbf{z}}_{c,h}) \equiv \sum_{\kappa \in \mathcal{T}_h} \bar{\eta}_{c,\kappa}, \quad (12)$$

where the adjoint-based indicators $|\bar{\eta}_{c,\kappa}|$ used within an adaptive mesh refinement algorithm are tailored to the accurate and efficient approximation of all target quantities $J_i(\mathbf{u})$ involved in the combined target quantity. The advantage of this approach of multi-target error estimation and adaptivity over the computation of an adjoint solution $\bar{\mathbf{z}}_{i,h} \in \mathbf{V}_h^{p+1}$ for each quantity $J_i(\mathbf{u})$, $i = 1, \dots, N$, is that it requires the solution of only one discrete adjoint problem (11) irrespective of the number N of target quantities (cf. [30] for more details).

Using the adjoint-based indicators, the elements in the computational mesh are identified and marked which contribute most to the error in the target quantity. In a (pure) mesh refinement (h -refinement) algorithm, simply all marked elements are refined by using element subdivision. In hp -refinement algorithms, the discrete solution on each marked element is further analyzed in order to decide whether to subdivide the element (h -refinement) or to increase the polynomial degree (p -refinement/enrichment). Here, the basic idea is to use high polynomial degrees and a coarse grid in smooth parts of the solution and to use low polynomial degrees and a refined mesh in non-smooth parts of the solution such as near shocks. To this end, the smoothness of the solution is estimated by analyzing the evolution of the coefficients of a Legendre series expansion of the solution [40]. If the coefficients decay rapidly, then the solution is assumed to be smooth and p -refinement is selected; if the coefficients decay slowly, then a non-smooth solution is assumed and h -refinement is selected. For more details on the hp -refinement approach used in this work, we refer to [27].

hp-refinement approach

4. GRADIENTS VIA THE ADJOINT APPROACH

Our optimization chain is driven by a gradient-based optimization algorithm, in particular the CG algorithm [32]. The gradients $\frac{dJ}{d\mathbf{D}}$ required, that is, the sensitivities of the objective function J to changes in the design variables \mathbf{D} , could be approximated using finite differences. Given the flow solution $\mathbf{U} = \mathbf{U}(\mathbf{D})$ for a given design $\mathbf{D} = (D_i)_{i=1}^n$, this, however, accounts to the computation of n additional flow solutions $\mathbf{U}(\mathbf{D} + \Delta\mathbf{D}_i)$, one for a change in each of the n design variables D_i . In this work, we employ an alternative approach, the so-called *adjoint approach* [1, 33], in which the gradient $\frac{dJ}{d\mathbf{D}}$ is computed based on the solution to the adjoint problem in (6) associated to the quantity J . Requiring the solution of a single auxiliary problem only, the adjoint approach of gradient evaluation is significantly more efficient than evaluating the gradients based on finite differences, in particular, in the case of a large number of design variables.

In many aerodynamic shape optimization problems, the lift is required to be kept constant. This lift constraint could be added as a penalty to the objective function [3], an approach also used in [19, 20]. We employ an alternative approach which ensures directly in the flow solver that the lift constraint is satisfied by adjusting the angle of attack during the flow solution process. This way, the target lift value C_L^* is made a solver parameter and replaces the angle of attack α . As the lift constraint has an impact on the adjoint-based gradient evaluation [2], we will recall the adjoint approach in the following subsections, first without and then including the target lift constraint.

4.1. Adjoint approach without lift constraint

Let us consider the following generic optimization problem:

$$\begin{aligned} & \text{minimize: } J(\mathbf{U}, X, \mathbf{D}), \\ & \text{subject to the constraint: } \mathbf{R}(\mathbf{U}, X, \mathbf{D}) = 0, \end{aligned} \quad (13)$$

where $J(\mathbf{U}, X, \mathbf{D})$ is the objective function such as the drag or lift coefficient (2), \mathbf{D} is the vector of design variables, $X = X(\mathbf{D})$ is the computational mesh, $\mathbf{U} = \mathbf{U}(X, \mathbf{D})$ is the coefficient vector of the flow solution, and $\mathbf{R} = \mathbf{R}(\mathbf{U}, X, \mathbf{D})$ is the residual vector introduced in Section 2.

Evaluating the gradient of the objective function and using chain rules, we obtain

$$\frac{dJ}{d\mathbf{D}} = \frac{\partial J}{\partial \mathbf{U}} \frac{d\mathbf{U}}{d\mathbf{D}} + \frac{\partial J}{\partial X} \frac{dX}{d\mathbf{D}} + \frac{\partial J}{\partial \mathbf{D}}. \quad (14)$$

Similarly, we obtain for the gradient of the residual vector

$$\frac{d\mathbf{R}}{d\mathbf{D}} = \frac{\partial \mathbf{R}}{\partial \mathbf{U}} \frac{d\mathbf{U}}{d\mathbf{D}} + \frac{\partial \mathbf{R}}{\partial X} \frac{dX}{d\mathbf{D}} + \frac{\partial \mathbf{R}}{\partial \mathbf{D}} = 0. \quad (15)$$

Introducing a Lagrange multiplier λ , the constrained minimization problem (13) can be solved by searching the stationary point of the Lagrange function

$$L(\mathbf{U}, X, \mathbf{D}) = J(\mathbf{U}, X, \mathbf{D}) + \lambda^\top \mathbf{R}(\mathbf{U}, X, \mathbf{D}). \quad (16)$$

As $\mathbf{R} = 0$ holds for all design variables \mathbf{D} , we have $J = L$, and thus obtain, using (14) and (15),

$$\begin{aligned} \frac{dJ}{d\mathbf{D}} = \frac{dL}{d\mathbf{D}} &= \left(\frac{\partial J}{\partial \mathbf{U}} \frac{d\mathbf{U}}{d\mathbf{D}} + \frac{\partial J}{\partial X} \frac{dX}{d\mathbf{D}} + \frac{\partial J}{\partial \mathbf{D}} \right) + \lambda^\top \left(\frac{\partial \mathbf{R}}{\partial \mathbf{U}} \frac{d\mathbf{U}}{d\mathbf{D}} + \frac{\partial \mathbf{R}}{\partial X} \frac{dX}{d\mathbf{D}} + \frac{\partial \mathbf{R}}{\partial \mathbf{D}} \right) \\ &= \left(\frac{\partial J}{\partial \mathbf{U}} + \lambda^\top \frac{\partial \mathbf{R}}{\partial \mathbf{U}} \right) \frac{d\mathbf{U}}{d\mathbf{D}} + \left(\frac{\partial J}{\partial X} + \lambda^\top \frac{\partial \mathbf{R}}{\partial X} \right) \frac{dX}{d\mathbf{D}} + \left(\frac{\partial J}{\partial \mathbf{D}} + \lambda^\top \frac{\partial \mathbf{R}}{\partial \mathbf{D}} \right). \end{aligned}$$

Here, the first term vanishes if λ is chosen to satisfy the following equation

$$\frac{\partial J}{\partial \mathbf{U}} + \lambda^\top \frac{\partial \mathbf{R}}{\partial \mathbf{U}} = 0, \quad (17)$$

which is equivalent to the adjoint equation in (6) including the adjoint solution vector λ . The remaining terms in the gradient are

$$\frac{dJ}{d\mathbf{D}} = \frac{dL}{d\mathbf{D}} = \left(\frac{\partial J}{\partial X} + \lambda^\top \frac{\partial \mathbf{R}}{\partial X} \right) \frac{dX}{d\mathbf{D}} + \left(\frac{\partial J}{\partial \mathbf{D}} + \lambda^\top \frac{\partial \mathbf{R}}{\partial \mathbf{D}} \right).$$

If the design variables are shape-based variables, then there is no direct dependence of J or \mathbf{R} on \mathbf{D} but only through $X = X(\mathbf{D})$. Thereby, the partial derivatives $\frac{\partial J}{\partial \mathbf{D}}$ and $\frac{\partial \mathbf{R}}{\partial \mathbf{D}}$ vanish.

Hence, we obtain the final gradient of the objective function with respect to design variables as

$$\frac{dJ}{d\mathbf{D}} = \left(\frac{\partial J}{\partial X} + \lambda^\top \frac{\partial \mathbf{R}}{\partial X} \right) \frac{dX}{d\mathbf{D}} = \frac{\partial J}{\partial X} \frac{dX}{d\mathbf{D}} + \lambda^\top \frac{\partial \mathbf{R}}{\partial X} \frac{dX}{d\mathbf{D}}. \quad (18)$$

The right-hand side of (18) can be approximated using finite differences

$$\begin{aligned} \left(\frac{\partial J}{\partial X} \frac{dX}{d\mathbf{D}} \right)_i &\approx \frac{J(\mathbf{U}, X(\mathbf{D} + \Delta \mathbf{D}_i), \mathbf{D}) - J(\mathbf{U}, X(\mathbf{D}), \mathbf{D})}{\Delta D_i}, \\ \left(\frac{\partial \mathbf{R}}{\partial X} \frac{dX}{d\mathbf{D}} \right)_i &\approx \frac{\mathbf{R}(\mathbf{U}, X(\mathbf{D} + \Delta \mathbf{D}_i), \mathbf{D}) - \mathbf{R}(\mathbf{U}, X(\mathbf{D}), \mathbf{D})}{\Delta D_i}, \end{aligned} \quad (19)$$

where ΔD_i is a perturbation of the design variable D_i . The terms $J(\mathbf{U}, X(\mathbf{D} + \Delta \mathbf{D}_i), \mathbf{D})$ and $\mathbf{R}(\mathbf{U}, X(\mathbf{D} + \Delta \mathbf{D}_i), \mathbf{D})$ are evaluated on each perturbed mesh obtained with mesh deformation. Note that they include the solution \mathbf{U} on the unperturbed mesh $X(\mathbf{D})$ and thus require no additional flow solutions.

Furthermore, note that introducing an additional mesh adjoint equation [7], the remaining terms on the right-hand side of (18) could be expressed via the additional adjoint variable allowing to circumvent the evaluation of finite differences. This, however, is beyond the scope of this work. Instead, we use the finite difference formulae (19) for approximating the gradient (18).

Finally, we note that the adjoint solution $\mathbf{z}_h \in \mathbf{V}_h^p$ involved in (18) via the adjoint solution vector $\boldsymbol{\lambda} = (\lambda_i)_{i=1}^N$ with $\mathbf{z}_h = \sum_{i=1}^N \lambda_i \boldsymbol{\phi}_i$ (recall Section 2) must be computed in the same function space as the flow solution, that is, $\mathbf{z}_h \in \mathbf{V}_h^p$ is the solution to (5) with $\bar{\mathbf{V}}_h^p = \mathbf{V}_h^p$. This is in contrast to the adjoint solutions $\bar{\mathbf{z}}_h$ and $\bar{\mathbf{z}}_{c,h} \in \mathbf{V}_h^{p+1}$ involved in the error estimation formulae and adjoint-based indicators, (9) and (12), which are computed with a polynomial degree $p + 1$ (recall Section 3). In fact, by numerical experiments, we have seen that evaluating (18) based on a $p + 1$ adjoint solution would result in an incorrect gradient (not shown for brevity). Therefore, in addition to the higher-order adjoint solutions $\bar{\mathbf{z}}_{c,h} \in \mathbf{V}_h^{p+1}$ required within the error estimation and adaptive mesh refinement algorithm, another adjoint solution $\mathbf{z}_h \in \mathbf{V}_h^p$ computed in the flow solution space \mathbf{V}_h^p is required for the gradient evaluation (18).

4.2. Adjoint approach with lift constraint

For a lift-constrained drag minimization problem, the constrained minimization problem (13) is replaced by

$$\begin{aligned} & \text{minimize: } \tilde{J}(\mathbf{U}, X, \mathbf{D}, \alpha), \\ & \text{subject to the constraints: } \mathbf{R}(\mathbf{U}, X, \mathbf{D}, \alpha) = 0, \\ & \quad \tilde{C}_L(\mathbf{U}, X, \mathbf{D}, \alpha) - C_L^* = 0, \end{aligned} \quad (20)$$

where the additional lift constraint will be satisfied through the variation of the angle of attack $\alpha = \alpha(\mathbf{D})$. Note that here, we use the notation $\tilde{J}(\mathbf{U}, X, \mathbf{D}, \alpha)$ to distinguish this objective function from $J = J(\mathbf{U}, X, \mathbf{D})$ in Section 4.1. Furthermore, note that we have

$$\frac{d\tilde{J}}{d\mathbf{D}} = \frac{dJ}{d\mathbf{D}} + \frac{d\tilde{J}}{d\alpha} \frac{d\alpha}{d\mathbf{D}}. \quad (21)$$

Ensuring directly in the flow solver that the lift constraint is satisfied by adjusting the angle of attack during the flow solution process, the target lift value C_L^* is made a solver parameter and replaces the angle of attack α . Thus, keeping the lift coefficient \tilde{C}_L constant, relation (21) for $\tilde{J} \equiv \tilde{C}_L$ gives

$$\frac{d\tilde{C}_L}{d\mathbf{D}} = \frac{dC_L}{d\mathbf{D}} + \frac{d\tilde{C}_L}{d\alpha} \frac{d\alpha}{d\mathbf{D}} = 0,$$

and thus,

$$\frac{d\alpha}{d\mathbf{D}} = -\frac{dC_L}{d\mathbf{D}} / \frac{d\tilde{C}_L}{d\alpha}. \quad (22)$$

Recalling that for a drag minimization problem, we have $\tilde{J} \equiv \tilde{C}_D$ in (21) and using (22) gives

$$\frac{d\tilde{C}_D}{d\mathbf{D}} = \frac{dC_D}{d\mathbf{D}} + \frac{d\tilde{C}_D}{d\alpha} \frac{d\alpha}{d\mathbf{D}} = \frac{dC_D}{d\mathbf{D}} - \left(\frac{d\tilde{C}_D}{d\alpha} / \frac{d\tilde{C}_L}{d\alpha} \right) \frac{dC_L}{d\mathbf{D}},$$

where in the following, we write $\frac{dC_D}{d\alpha}$ for $\frac{d\tilde{C}_D}{d\alpha}$ and $\frac{dC_L}{d\alpha}$ for $\frac{d\tilde{C}_L}{d\alpha}$ for simplicity, that is,

$$\frac{d\tilde{C}_D}{d\mathbf{D}} = \underbrace{\frac{dC_D}{d\mathbf{D}}}_{\text{base}} - \underbrace{\left(\frac{dC_D}{d\alpha} / \frac{dC_L}{d\alpha} \right) \frac{dC_L}{d\mathbf{D}}}_{\text{correction}}, \quad (23)$$

(cf. [2]). The sensitivities of the force coefficients to the design variables \mathbf{D} , that is, $\frac{dC_D}{d\mathbf{D}}$ and $\frac{dC_L}{d\mathbf{D}}$, can be computed according to (18), whereas the sensitivities to the angle of attack can be evaluated based on finite differences, for example, by the forward finite difference method

$$\frac{dC_D}{d\alpha} \approx \frac{C_D(\mathbf{U}(\alpha + \Delta\alpha), X, \mathbf{D}, \alpha + \Delta\alpha) - C_D(\mathbf{U}(\alpha), X, \mathbf{D}, \alpha)}{\Delta\alpha}$$

and accordingly for $\frac{dC_L}{d\alpha}$. Given the flow solution $\mathbf{U} = \mathbf{U}(\alpha)$, the computation of $\mathbf{U}(\alpha + \Delta\alpha)$ for a small $\Delta\alpha > 0$ requires very few additional flow solver iteration steps, only.

From (23), we see that for a target lift computation, the *correction* term $-\left(\frac{dC_D}{d\alpha} / \frac{dC_L}{d\alpha}\right) \frac{dC_L}{d\mathbf{D}}$ must be added to the *base* gradient $\frac{dC_D}{d\mathbf{D}}$, which is computed according to (18) where a fixed angle of attack is assumed.

4.3. Verification of the gradients

The verification of the gradients obtained with the gradient approach against those obtained with finite differences has been performed on uniform meshes many times in literature [2, 3, 5, 10, 41] among many other. Omitting here intermediate verification steps for brevity, in the following, we show the verification of the gradients when both mesh refinement and a target lift constraint are under consideration. The test case considered is based on a transonic inviscid flow around the RAE2822 airfoil at Mach = 0.734 where the target lift is kept constant at 0.8. The RAE2822 airfoil is parametrized using 20 Hicks–Henne functions [42]. The DG flow solver PADGE [23] is used to compute the flow solutions and adjoint solutions of the same polynomial degree on a sequence of meshes which are adaptively refined targeted at the accurate and efficient computation of both the drag and lift coefficients (cf. the multi-target adjoint-based mesh refinement described in Section 3 with equal weighting factors, $\alpha_1 = \alpha_2 = 1$, in (10)).

Figure 1(a,b) shows the verification on an h -refined mesh and on an hp -refined mesh, respectively. Here, a gradient computed using the adjoint solution (in green) is obtained by adding the correction

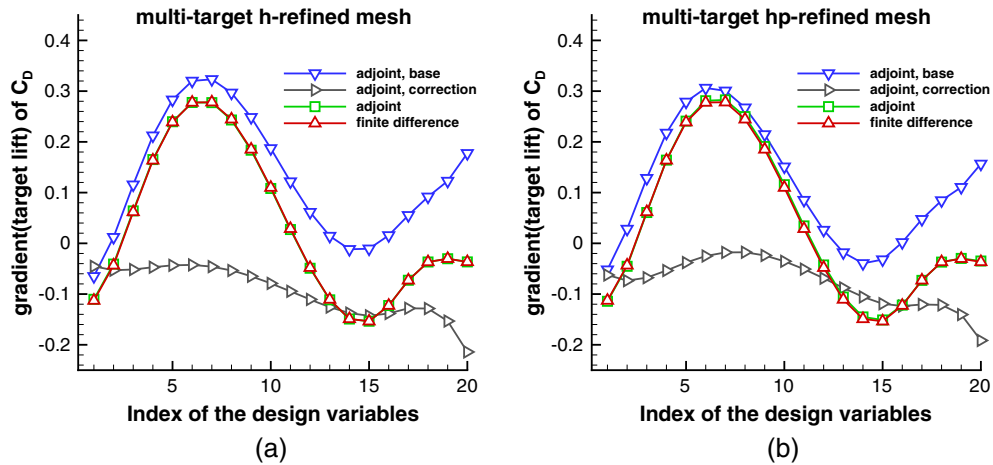


Figure 1. Gradients of the drag coefficient computed using the adjoint approach compared with finite differences when target lift and multi-target mesh refinement are under consideration: (a) on h -refined mesh, (b) on hp -refined mesh.

term (in black) to the base gradient (in blue) according to (23). We see that the gradients computed using the adjoint approach (in green) match very well the gradients obtained using finite differences (in red).

5. SHAPE OPTIMIZATION OF THE RAE2822 AIRFOIL

In the following, we consider a shape optimization problem based on an inviscid transonic flow at Mach number $M = 0.734$ around the RAE2822 airfoil. Keeping the thickness of the profile frozen, the goal of the optimization is to change the shape of the profile such as to minimize the drag at a constant lift coefficient of 0.8. Although the transonic flow around the original shape given by the RAE2822 airfoil features a strong shock, we expect that the shape would be modified such that the shock strength and thus the drag reduce until the shock is possibly removed. For this kind of test case, the success of the optimization can easily be judged according to whether the shock is removed or not and by the value of the remaining drag which ideally would vanish. Similar lift-constrained shape optimization problems have already been considered in [22, 43, 44].

In this section, the RAE2822 airfoil is parametrized using 15 Hicks–Henne functions. An original structured mesh around the RAE2822 airfoil with 8192 straight-sided elements is agglomerated twice resulting in a coarse mesh of 512 elements which is curved with quartic polynomials based on the points removed from the original mesh. The airfoil shape represented by this coarse curved mesh will not be changed under subsequent mesh refinement. All flow and adjoint computations have been performed using the DG flow solver PADGE [23]. The lift constraint is realized by an automatic adjustment of the angle of attack during the flow solution process. The optimization is driven by the CG algorithm [32] where the gradients are computed using the adjoint approach as described in Section 4. Finally, the deformation of the original mesh to new airfoil shapes as well as the perturbation of the mesh for computing (19) is realized using the DLR-TAU mesh deformation [45, 46].

First, we apply the optimization algorithm to the second-order DG discretization on a uniform fine mesh of 32,768 elements which is obtained after three global refinement steps of the coarse mesh with 512 curved elements. The optimization result on this fixed mesh serves as a baseline computation and will later be compared with optimization results obtained on h -refined and hp -refined meshes with different error levels prescribed. Note that according to the different discretization errors involved, also the airfoil shapes obtained in the different optimization runs may be different. In order to judge the quality of the optimized airfoil shapes, we perform a grid refinement study for each them. In particular, we obtain accurate drag coefficient values of the optimized airfoil shapes by recomputing the flow solution on locally refined very fine meshes. To this end, we employ the adjoint-based mesh refinement (cf. Section 3) targeted at the accurate evaluation of the drag coefficient until the error estimation indicates a discretization error in the drag coefficient of less than 5×10^{-5} . The optimized airfoil shape and the corresponding recomputed c_p -distribution are shown in Figure 2 in comparison with those of the initial RAE2822 airfoil. Here, we see that the constraint on the thickness of the airfoil is satisfied. Furthermore, the shock located on the upper side of the initial airfoil is significantly reduced on the optimized airfoil shape. However, there are still some disturbances visible in the c_p -distributions near the original shock location. We note that already some small disturbances are visible in the c_p -distribution computed on the fixed mesh (not shown), which, however, amplifies like seen in 2(b) in the grid convergence study. This indicates that the fixed fine mesh is not sufficiently fine for accurately approximating the flow solution close to the initial shock location. Correspondingly, the drag coefficient of the optimized airfoil shape on the fixed fine mesh is given by 0.000278 but is increased to 0.000306 in the grid convergence study. Still, this corresponds to a drag reduction at constant lift of about 95% compared with the initial airfoil shape given by the RAE2822 airfoil, for which a grid refinement study gives a drag coefficient of 0.005907. Table I collects the drag, lift, and moment coefficients C_D , C_L , and C_M , and the angle of attack α at which the target lift 0.8 is obtained on the fixed fine mesh and those obtained in the grid convergence study. Here, the first line includes the data of the initial airfoil shape, whereas the second line includes the data of the airfoil shape optimized on the fixed mesh. Here, also, the

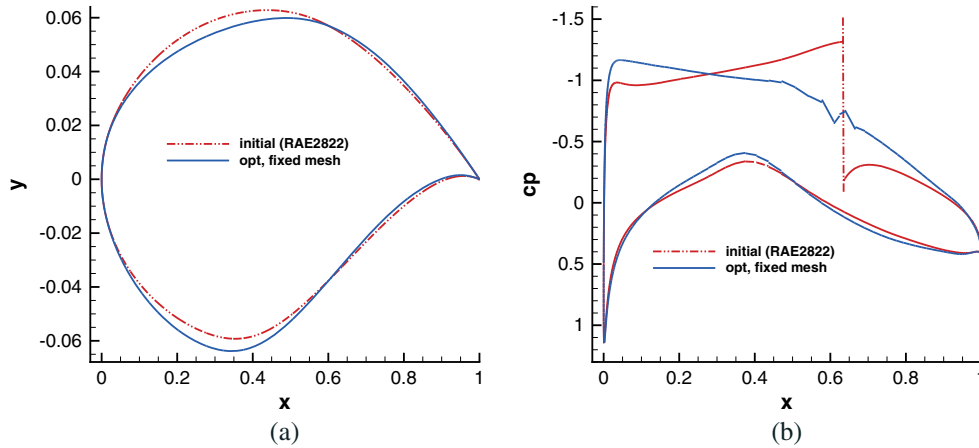


Figure 2. (a) Comparison of the initial airfoil shape and the final optimized shape on the fixed mesh with 32,768 elements and (b) comparison of the corresponding recomputed c_p -distributions.

Table I. Optimization results on h -refined meshes.

	Optimization results					Grid converged values			
	C_D	C_L	α	dofs/eqn	Cost	C_D	C_L	C_M	α
Initial	-	-	-	-	-	0.005907	0.8000	0.1310	1.666
Fixed mesh	0.000278	0.7994	1.581	98304	1.00	0.000306	0.7998	0.1308	1.587
e. tol=5e-2	0.003217	0.8000	2.029	~ 4170	0.08	0.001372	0.8000	0.1079	2.013
e. tol=1e-2	0.004984	0.8004	1.689	~ 6750	0.07	0.004325	0.7998	0.1285	1.680
e. tol=5e-3	0.001110	0.8009	1.613	~ 11120	0.15	0.000780	0.8002	0.1280	1.607
e. tol=1e-3	0.000490	0.8005	1.563	~ 18800	0.21	0.000344	0.8000	0.1325	1.563
e. tol=5e-4	0.000347	0.7998	1.571	~ 31070	0.82	0.000300	0.7998	0.1314	1.575

number of degrees of freedom per equation (#dofs/eqn) is given, which is 98,304 for the second-order DG discretization, that is, $\mathbf{u}_h \in \mathbf{V}_h^p$ with $p = 1$ in (4), on the uniform fine mesh of 32,768 elements. Note that due to the 2D coordinate system used in the flow computations, a positive moment corresponds to a nose down pitching. Furthermore, note that the moment coefficient may change during the optimization as it is not considered a constraint in the optimization problem.

The next (i.e., third) line in Table I collects the optimization result obtained on h -refined meshes for a prescribed discretization error tolerance of 5×10^{-2} . Here, the flow computation required in each optimization step is computed on a sequence of adaptively refined meshes. Each flow computation is started on the coarse mesh with 512 curved elements. This mesh is then successively refined using the multi-target error estimation and adaptation algorithm (cf. Section 3 and [30]) targeted at the accurate and efficient approximation of both the drag and lift coefficients. This local mesh refinement algorithm is proceeded until the error estimate (12) is below the prescribed error tolerance of 5×10^{-2} . Note that for each airfoil shape considered in the optimization process, a different sequence of locally refined meshes is created. In fact, each mesh sequence is particularly tailored to the accurate and efficient computation of the drag and lift coefficients of the airfoil shape currently at hand. However, note that drag coefficients obtained in the different steps of the optimization loop are still comparable as each of them is subject to a discretization error in the drag and lift coefficients of the same error level. In the third line of Table I, we see that the resulting optimized airfoil shape gives a drag coefficient of 0.003217 computed on the locally adapted but still very coarse mesh, but the grid refinement study reveals a drag coefficient of 0.001372 which corresponds to a drag reduction of about 77% compared with that of the initial RAE2822 airfoil. With the rather high discretization error tolerance of 5×10^{-2} prescribed, the final adapted meshes are rather coarse, the flow solution is very cheap but also quite inaccurate. In fact, the resulting 77% of

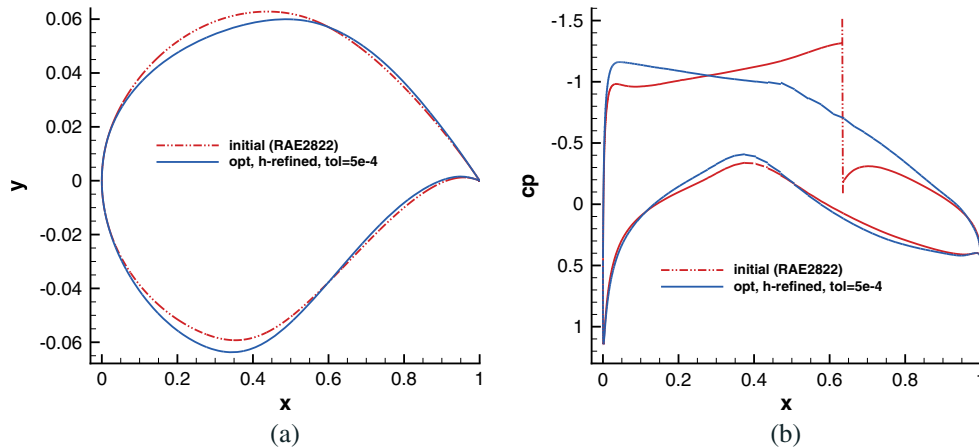


Figure 3. (a) Comparison of the initial airfoil shape and the final optimized shape obtained on h -refined meshes (error tol. of 5×10^{-4}) and (b) comparison of the corresponding recomputed c_p -distributions.

drag reduction is much less than the 95% reduction obtained on the fixed fine mesh. However, the approximately 4170 degrees of freedom (DOF) per equation for the α -order DG solution on the final adapted meshes are much less than the 98,304 on the fixed fine mesh. Furthermore, the computing time on the h -refined mesh is only about 8% of that on the fixed fine mesh (cf. Table I, column 6).

The next lines in Table I collect the corresponding data of the optimization results obtained on h -refined meshes for lower discretization error tolerances 10^{-2} , 5×10^{-3} , 10^{-3} , and 5×10^{-4} . First, we note that although the error tolerance decreases, the number of DOF on the final adapted meshes and also the computing time increases. Furthermore, we see, that except for a single outlier at 10^{-2} , the optimal drag coefficient C_D reduces as the error tolerance decreases. This corresponds to an improved quality of the optimal airfoil shapes as the accuracy of the underlying flow solutions is improved. Finally, we see that for the error tolerance 5×10^{-4} , the optimal drag coefficient is slightly smaller than that on the fixed mesh, whereas the optimization process on the h -refined meshes takes only about 82% of the computing time of that on the fixed mesh.

For the error tolerance 5×10^{-4} , the resulting airfoil shape and the recomputed c_p -distribution are shown in Figure 3 in comparison with those of the initial RAE2822 airfoil. Here, the shock located on the upper side of the initial airfoil is almost completely eliminated on the optimized airfoil shape. In particular, we see a clear difference to the recomputed c_p -distribution of the airfoil shape optimized on the fixed mesh (compare Figure 3(b) with Figure 2(b)). This indicates that the flow solutions on the h -refined meshes are sufficiently accurate to lead the optimization algorithm to a good airfoil shape with a smooth c_p -distribution, whereas the flow solutions on the fixed fine mesh were not.

We recall that the force coefficients collected in columns 7–10 of Table I are evaluated through a grid convergence study of the optimized shapes using an adjoint-based mesh refinement algorithm targeted at the accurate computation of the drag coefficient. The locally refined meshes for the initial RAE2822 airfoil and for the optimized shape at error tolerance 5×10^{-4} are shown in Figure 4(a,b). In addition to mesh refinement near the leading and trailing edge, in Figure 4(a), we see some refinement of the shock close to the airfoil. Furthermore, there is some refinement on a line starting from the point where the shock touches the airfoil. This line represents a characteristic of the adjoint solution and underlines the importance of the influence of the position of the shock on the resulting drag coefficient. This kind of adaptive mesh refinement is typical for transonic flows when adjoint-based indicators are used (cf. e.g., [47]). In contrast to that, there is no significant refinement at the corresponding position in Figure 4(b), which corresponds to the fact that here, the flow solution is smooth.

Whereas Table I includes the optimization results on the h -refined meshes with specific error tolerances described, Table II includes the corresponding optimization results on hp -refined meshes. Again, with a single outlier at the error tolerance 5×10^{-3} , we see that the optimized drag coefficient

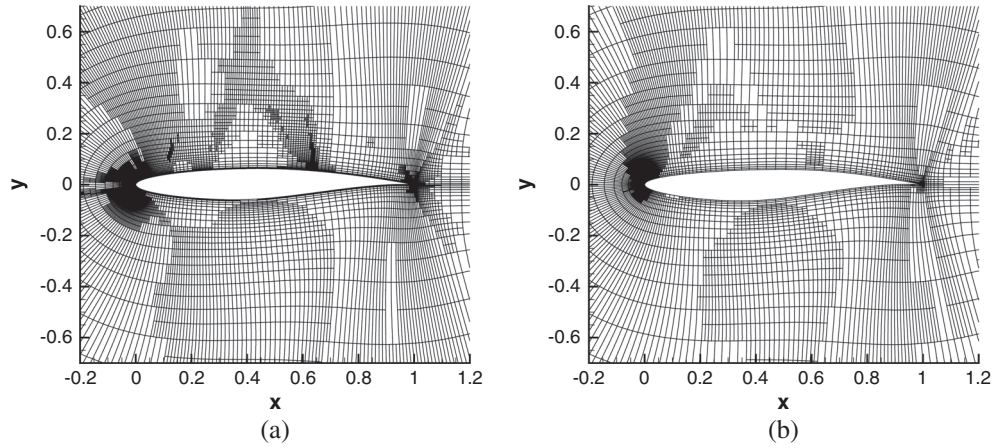


Figure 4. Adjoint-based refined meshes obtained in the grid convergence study for (a) the initial RAE2822 airfoil and (b) the airfoil shape optimized on h -refined meshes (with error tolerance of 5×10^{-4}).

Table II. Optimization results on hp -refined meshes.

	Optimization results					Grid converged values			
	C_D	C_L	α	dofs/eqn	Cost	C_D	C_L	C_M	α
Initial	-	-	-	-	-	0.005907	0.8000	0.1310	1.666
Fixed mesh	0.000278	0.7994	1.581	98304	1.00	0.000306	0.7998	0.1308	1.587
e. tol= $5e-2$	0.003513	0.8000	1.543	~ 3510	0.05	0.000755	0.8003	0.1380	1.460
e. tol= $1e-2$	0.001672	0.8000	1.510	~ 4180	0.10	0.000366	0.8002	0.1305	1.584
e. tol= $5e-3$	0.001153	0.8000	1.592	~ 4800	0.13	0.000410	0.8016	0.1305	1.588
e. tol= $1e-3$	0.000414	0.8001	1.549	~ 6670	0.24	0.000365	0.8003	0.1335	1.549
e. tol= $5e-4$	0.000309	0.8001	1.508	~ 10050	0.29	0.000300	0.8002	0.1341	1.513

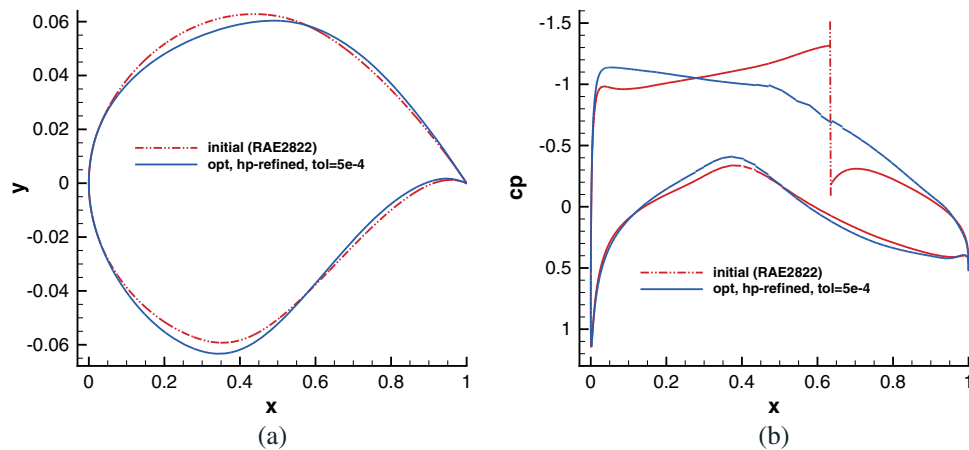


Figure 5. (a) Comparison of the initial airfoil shape and the final optimized shape obtained on hp -refined meshes (error tol. of 5×10^{-4}) and (b) comparison of the corresponding recomputed c_p -distributions.

decreases as the prescribed error tolerance decreases. This corresponds to an increased quality of the optimized airfoil shape for an increased accuracy of the underlying flow solutions. Furthermore, the drag coefficient of 0.0003 for the airfoil shape optimized on the hp -refined meshes with an error tolerance of 5×10^{-4} is smaller than that for the shape optimized on the fixed fine mesh, whereas

the optimization process on the hp -refined meshes takes only about 29% of the computing time of that on the fixed mesh.

For the error tolerance 5×10^{-4} , the resulting airfoil shape and the recomputed c_p -distribution are shown in Figure 5 in comparison with those of the initial RAE2822 airfoil. Here, like in Figure 3(b), the shock located on the upper side of the initial airfoil is almost completely eliminated on the

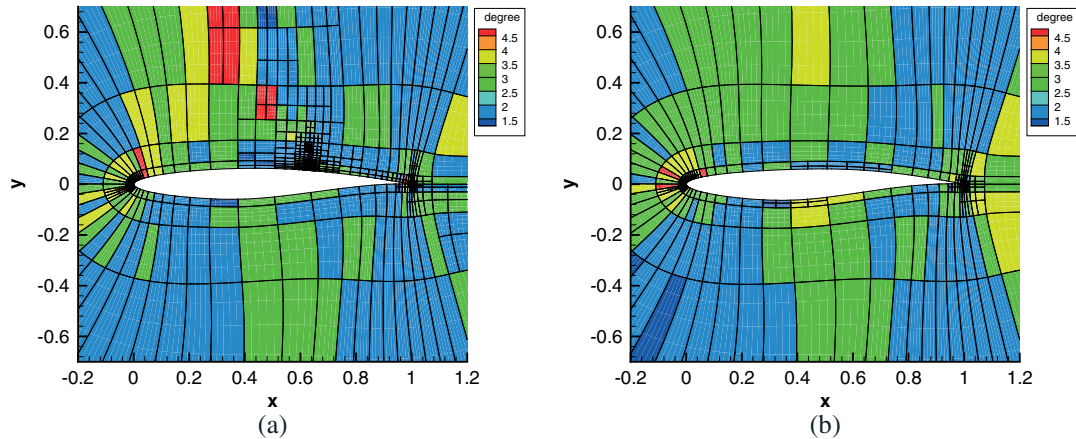


Figure 6. Adjoint-based hp -refined meshes with an error tolerance of 5×10^{-4} for (a) the initial RAE2822 airfoil and (b) the airfoil shape optimized on hp -refined meshes (error tol. of 5×10^{-4}).

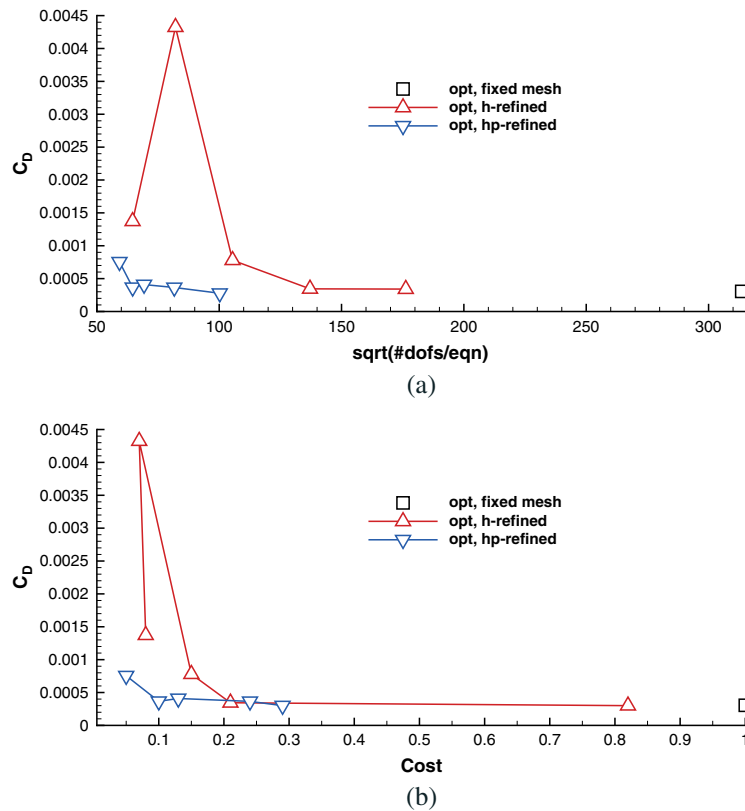


Figure 7. Optimized drag coefficient values obtained on the fixed mesh and on the h -refined and the hp -refined meshes for different error tolerances over (a) the (square root of the) number of degrees of freedom per equation and (b) the computational cost.

optimized airfoil shape. This indicates that the hp -refined meshes are sufficiently accurate to lead the optimization algorithm to a good airfoil shape with smooth c_p -distribution. The hp -refined meshes obtained through the adjoint-based mesh refinement algorithm targeted at accurately approximating both the drag and lift coefficients are shown in Figure 6(a,b) for the initial and the optimized airfoil shape, respectively. In Figure 6(a), we see that local h -refinement, that is, element subdivision, is performed in non-smooth parts of the flow solution near the leading and the trailing edge and in particular near the shock on the upper side of the profile. In the rest of the elements chosen for refinement, the flow solution is smooth and the polynomial degree is increased. Also in Figure 6(b), there is local h -refinement close to the leading and trailing edges. However, here, almost no h -refinement is performed near the initial shock location corresponding to the fact that here, the flow solution is smooth. We note that the adjoint-based h -refined meshes created along the grid convergence study are similar to those in Figure 4 and are not shown for brevity.

Finally, in Figure 7, we compare the drag coefficients of the optimized airfoil shapes obtained in the optimization processes on hp -refined meshes (in blue) with those obtained on h -refined meshes (in red) and that obtained on the fixed fine mesh (in black). Figure 7(a) plots the optimal drag coefficients over the square root of the number of DOF per equation, $\sqrt{\#\text{dofs}/\text{eqn}}$, which corresponds to a mean grid size h in h -refined meshes in two dimensions. Here, we see that using h -refinement, good airfoil shapes are obtained with significantly less DOF than on the fixed fine mesh. Moreover, hp -refinement gives a further significant reduction in the number of DOF. As we see in Figure 7(b), this also transfers to a significant reduction in the computational cost.

6. CONCLUSION

Based on a DG flow and adjoint solver, we built a gradient-based optimization algorithm where the gradients of the objective function including the treatment of a target lift constraint are evaluated using the adjoint approach. Applied on an inviscid flow around the RAE2822 airfoil at transonic flow conditions, we obtained a reduction in the drag of the airfoil shape at constant lift of about 95% when the flow computations are performed on a fixed uniformly fine mesh. In addition, we devised a new optimization algorithm, where each flow computation is performed on a sequence of goal-oriented h -refined or hp -refined meshes until the error estimation of the discretization error in a flow-related target quantity (including the drag and lift coefficients) is below a prescribed error tolerance. We have seen that the quality of the resulting optimized airfoil shape depends on the error tolerance prescribed. In fact, except for single outliers related to particularly weak accuracy requirements, the quality of the optimized shapes increases as the error tolerance decreases, and the accuracy of the flow solutions increases. With an error tolerance of $5 \cdot 10^{-4}$, the optimization based on the h -refined meshes and the hp -refined meshes gave a slightly lower optimal drag coefficient than the optimization on the fixed uniform fine mesh. Here, the drag coefficients of all optimized airfoil shapes were recomputed based on a grid convergence study. Furthermore, the recomputed c_p -distributions of the airfoil shapes optimized on the h -refined and the hp -refined meshes were smooth, whereas that optimized on the fixed fine mesh was not. Finally, in addition to resulting in better airfoil shapes, the computing time on the h -refined meshes was 82% and that on hp -refined meshes was only 29% of the computing time on the fixed uniform mesh.

REFERENCES

1. Jameson A. Optimum aerodynamic design using CFD and control theory. *12th Computational Fluid Dynamics Conference*, AIAA Paper 95-1729, San Diego, California, 1995.
2. Reuther JJ, Jameson A, Alonso JJ, Rimlinger MJ, Saunders D. Constrained multipoint aerodynamic shape optimization using an adjoint formulation and parallel computers, part 1. *Journal of Aircraft* 1999; **36**(1):51–60.
3. Anderson WK, Venkatakrishnan V. Aerodynamic design optimization on unstructured grids with a continuous adjoint formulation. *Computers and Fluids* 1999; **28**:443–480.
4. Giles MB, Pierce NA. An introduction to the adjoint approach to design. *Flow, Turbulence and Combustion* 2000; **65**(3-4):393–415.

5. Kim S, Alonso JJ, Jameson A. Multi-element high-lift configuration design optimization using viscous continuous adjoint method. *Journal of Aircraft* 2004; **41**(5):1082–1097.
6. Mavriplis D. A discrete adjoint-based approach for optimization problems on three-dimensional unstructured meshes. *44th AIAA Aerospace Sciences Meeting and Exhibit*, AIAA 2006-50, Reno, Nevada, 2006.
7. Nielsen EJ, Park MA. Using an adjoint approach to eliminate mesh sensitivities in computational design. *AIAA Journal* 2006; **44**(5):948–953.
8. Papadimitriou DI, Giannakoglou KC. Aerodynamic design using the truncated Newton algorithm and the continuous adjoint approach. *International Journal for Numerical Methods in Fluids* 2011; **68**(6):724–739. DOI: 10.1002/fld.2530.
9. Brezillon J, Abu-Zurayk M. Aerodynamic inverse design framework using discrete adjoint method. In *New Results in Numerical and Experimental Fluid Mechanics VIII: Contributions to the 17th STAB/DGLR Symposium Berlin, Germany, 2010*, vol. 121, Dillmann A, Heller G, Kreplin H-P, Nitsche W, Peltzer I (eds.), Notes on Numerical Fluid Mechanics and Multidisciplinary Design. Springer: Berlin Heidelberg, 2013; 489–496. DOI: 10.1007/978-3-642-35680-3_59.
10. Schmidt S, Ilic C, Schulz V, Gauger N. Three-dimensional large-scale aerodynamic shape optimization based on shape calculus. *AIAA Journal* 2013; **51**(11):2615–2627. DOI: 10.2514/1.J052245.
11. Bassi F, Rebay S. High-order accurate discontinuous finite element solution of the 2d Euler equations. *Journal of Computational Physics* 1997; **138**:251–285.
12. Cockburn B, Karniadakis GE, Shu C-W (eds.) *Discontinuous Galerkin Methods*, Lecture Notes in Computational Science and Engineering, vol. 11. Springer: Berlin Heidelberg, 2000.
13. Hesthaven JS, Warburton T. *Nodal Discontinuous Galerkin Methods*, Texts in Applied Mathematics, vol. 54. Springer: Berlin Heidelberg, 2008.
14. Fidkowski KJ, Darmofal DL. Review of output-based error estimation and mesh adaptation in computational fluid dynamics. *AIAA Journal* 2011; **49**(4):673–694.
15. Hartmann R, Leicht T. Higher order and adaptive DG methods for compressible flows. In *VKI LS 2014-03: 37th Advanced CFD Lecture Series: Recent Developments in Higher Order Methods and Industrial Application in Aeronautics, Dec. 9-12, 2013*, Deconinck H, Abgrall R (eds). Von Karman Institute for Fluid Dynamics: Rhode Saint Genèse, Belgium, 2014.
16. Becker R. Mesh adaptation for stationary flow control. *Journal of Mathematical Fluid Mechanics* 2001; **3**(4): 317–341.
17. Becker R, Heuveline V, Rannacher R. An optimal control approach to adaptivity in computational fluid mechanics. *International Journal for Numerical Methods in Fluids* 2002; **40**:105–120. DOI: 10.1002/fld.269.
18. Lu J. An a posteriori error control framework for adaptive precision optimization using discontinuous Galerkin finite element method. *Ph.D. Thesis*, M.I.T., 2005.
19. Lu J, Darmofal DL. Adaptive precision methodology for flow optimization via output error control. *42nd AIAA Aerospace Sciences Meeting and Exhibit*, AIAA 2004-1096, Reno, Nevada, 2004.
20. Nemec M, Aftosmis MJ. Output error estimates and mesh refinement in aerodynamic shape optimization. *51st AIAA Aerospace Sciences Meeting*, AIAA 2013-0865, Grapevine, Texas, 2013.
21. Mohammadi B, Hecht F. Mesh adaptation for time dependent simulation, optimization and control. *Revue Européenne des Éléments Finis* 2001; **10**(5):575–593.
22. Kouhi M, Bugada G, Lee D, Oñate E. Aerodynamic shape optimization using adaptive remeshing. *2nd International Conference on Engineering Optimization*, Lisbon, Portugal, September 6-9, 2010.
23. Hartmann R, Held J, Leicht T, Prill F. Discontinuous Galerkin methods for computational aerodynamics – 3D adaptive flow simulation with the DLR PADGE code. *Aerospace Science and Technology* 2010; **14**:512–519. DOI: 10.1016/j.ast.2010.04.002.
24. Kroll N. ADGIMA – a European project on the development of adaptive higher-order variational methods for aerospace applications. *47th AIAA Aerospace Sciences Meeting*, AIAA 2009-176, Orlando, Florida, 2009.
25. Wang ZJ (ed.) *Adaptive High-Order Methods in Computational Fluid Dynamics*, Advances in Computational Fluid Dynamics, vol. 2. World Science Books, 2011. (Available from: <http://www.worldscibooks.com/mathematics/7792.html>) [Accessed on March 2011].
26. Wang ZJ, Fidkowski K, Abgrall R, Bassi F, Caraeni D, Cary A, Deconinck H, Hartmann R, Hillewaert K, Huynh HT, Kroll N, May G, Persson PO, van Leer B, Visbal M. High-order CFD methods: current status and perspective. *International Journal for Numerical Methods in Fluids* 2013; **72**(8):811–845. DOI: 10.1002/fld.3767.
27. Leicht T, Hartmann R. Error estimation and *hp*-adaptive mesh refinement for discontinuous Galerkin methods. In *Adaptive High-Order Methods in Computational Fluid Dynamics*, vol. 2, Wang ZJ (ed.), chap. 3. World Science Books, 2011; 67–94. (Available from: <http://www.worldscibooks.com/mathematics/7792.html>) [Accessed on March 2011].
28. Wang L, Mavriplis DJ. Adjoint-based *h-p* adaptive discontinuous Galerkin methods for the 2D compressible Euler equations. *Journal of Computational Physics* 2009; **228**(20):7643–7661.
29. Hartmann R, Houston P. Adaptive discontinuous Galerkin finite element methods for the compressible Euler equations. *Journal of Computational Physics* 2002; **183**(2):508–532. DOI: 10.1006/jcph.2002.7206.
30. Hartmann R. Multitarget error estimation and adaptivity in aerodynamic flow simulations. *SIAM Journal of Scientific Computing* 2008; **31**(1):708–731. DOI: 10.1137/070710962.

31. Leicht T, Hartmann R. Error estimation and anisotropic mesh refinement for 3d laminar aerodynamic flow simulations. *Journal of Computational Physics* 2010; **229**(19):7344–7360. (Available from: <http://dx.doi.org/10.1016/j.jcp.2010.06.019>) [Accessed on 20 September 2010].
32. Knyazev AV, Lashuk I. Steepest descent and conjugate gradient methods with variable preconditioning. *SIAM Journal on Matrix Analysis and Applications* 2008; **29**(4):1267–1280.
33. Jameson A. Aerodynamic design via control theory. *Journal of Scientific Computing* 1988; **3**:233–260.
34. Hartmann R. Adjoint consistency analysis of discontinuous Galerkin discretizations. *SIAM Journal on Numerical Analysis* 2007; **45**(6):2671–2696.
35. Eriksson K, Estep D, Hansbo P, Johnson C. Introduction to adaptive methods for differential equations. *Acta Numerica* 1995; **4**:105–158.
36. Becker R, Rannacher R. A feed-back approach to error control in finite element methods: Basic analysis and examples. *East–West Journal on Numerical Mathematics* 1996; **4**:237–264.
37. Becker R, Rannacher R. An optimal control approach to a posteriori error estimation in finite element methods. *Acta Numerica* 2001; **10**:1–102.
38. Pierce NA, Giles MB. Adjoint recovery of superconvergent functionals from PDE approximations. *SIAM Review* 2000; **42**(2):247–264.
39. Giles MB, Süli E. Adjoint methods for PDEs: a posteriori error analysis and postprocessing by duality. *Acta Numerica* 2002; **11**:145–236.
40. Mavriplis C. Adaptive mesh strategies for the spectral element method. *Computer Methods in Applied Mechanics and Engineering* 1994; **116**:77–86.
41. Brezillon J, Gauger N. 2D and 3D aerodynamic shape optimisation using the adjoint approach. *DGLR Jahrbuch 2003, Band 1, Deutscher Luft- und Raumfahrtkongress*, München, November 17–20, 2003; 87–96.
42. Hicks RM, Henne PA. Wing design by numerical optimization. *Journal of Aircraft* 1978; **15**:407–412.
43. Brezillon J, Gauger N. 2D and 3D aerodynamic shape optimisation using the adjoint approach. *Aerospace Science and Technology* 2004; **8**:715–727.
44. Schmidt S, Ilıc C, Schulz V, Gauger NR. Airfoil design for compressible inviscid flow based on shape calculus. *Engineering Optimization* 2011; **12**:349–369. DOI: 10.1007/s11081-011-9145-3.
45. Schwamborn D, Gerhold T, Heinrich R. The DLR TAU-code: Recent applications in research and industry. *Proceedings of the European Conference on Computational Fluid Dynamics ECCOMAS CFD*, 2006. (Available from: <http://proceedings.fyper.com/eccomascfd2006/documents/619.pdf>) [Accessed on 2006].
46. Gerhold T, Neumann J. The parallel mesh deformation of the DLR-TAU-code. In *Notes on numerical fluid mechanics and multidisciplinary design*, P. Wesseling, E. Oñate, J. Périaux (eds). Springer: Berlin Heidelberg, 2007; 162–169. ISBN 3-540-74458-4.
47. Leicht T, Hartmann R. Anisotropic mesh refinement for discontinuous Galerkin methods in two-dimensional aerodynamic flow simulations. *International Journal for Numerical Methods in Fluids* 2008; **56**(11): 2111–2138.